JACS JOURNAL OF THE AMERICAN CHEMICAL SOCIETY

Article

Cite This: J. Am. Chem. Soc. 2017, 139, 14501-14510

pubs.acs.org/JACS

Probing Frontier Orbital Energies of $\{Co_9(P_2W_{15})_3\}$ Polyoxometalate Clusters at Molecule–Metal and Molecule–Water Interfaces

Xiaofeng Yi,[†,‡] Natalya V. Izarova,[†] Maria Stuckart,[†,‡] David Guérin,[§] Louis Thomas,[§] Stéphane Lenfant,[§] Dominique Vuillaume,*[,§] Jan van Leusen,[‡] Tomáš Duchoň,[∥] Slavomír Nemšák,[†,¶] Svenja D. M. Bourone,[‡] Sebastian Schmitz,[‡] and Paul Kögerler*[,†,‡]

[†]Jülich-Aachen Research Alliance (JARA-FIT) and Peter Grünberg Institute 6, Forschungszentrum Jülich, D-52425 Jülich, Germany

[‡]Institute of Inorganic Chemistry, RWTH Aachen University, D-52074 Aachen, Germany

[§]Institute of Electronics, Microelectronics and Nanotechnology, CNRS, University of Lille, 59652 Villeneuve d'Ascq, France

[∥]Faculty of Mathematics and Physics, Charles University, 18000 Prague, Czech Republic

[¶]BESSY-II, Helmholtz-Zentrum Berlin, D-12489 Berlin, Germany

Supporting Information

ABSTRACT: Functionalization of polyoxotungstates with organoarsonate coligands enabling surface decoration was explored for the triangular cluster architectures of the composition $[Co^{II}_9(H_2O)_6(OH)_3(p\text{-}RC_6H_4As^{V}O_3)_2(\alpha\text{-}P^{V}_2W^{VI}_{15}O_{56})_3]^{25-}$ ($\{Co_9(P_2W_{15})_3\}$, R = H or NH_2), isolated as $Na_{25}[Co_9(OH)_3(H_2O)_6(C_6H_5AsO_3)_2(P_2W_{15}O_{56})_3]\cdot 86H_2O$ (**Na-1**; triclinic, $P\bar{1}$, a = 25.8088(3) Å, b = 25.8336(3) Å, c = 27.1598(3) Å, α = 78.1282(11)°, β = 61.7276(14)°, γ = 60.6220(14)°, V = 13888.9(3) Å^3, Z = 2) and $Na_{25}[Co_9(OH)_3(H_2O)_6(H_2NC_6H_4AsO_3)_2(P_2W_{15}O_{56})_3]\cdot 86H_2O$ (**Na-2**; triclinic, $P\bar{1}$, a = 14.2262(2) Å, b = 24.8597(4) Å, c = 37.9388(4) Å, α = 81.9672(10)°, β = 87.8161(10)°, γ = 76.5409(12)°, V = 12920.6(3) Å^3, Z = 2). The axially oriented *para*-aminophenyl groups in **2** facilitate the formation of self-assembled monolayers on gold surfaces and thus provide a viable molecular platform for charge transport studies of magnetically functionalized polyoxometalates. The title systems were isolated and characterized in the solid state, in aqueous solutions, and on metal surfaces. Using conducting tip atomic force microscopy, the energies of $\{Co_9(P_2W_{15})_3\}$ frontier molecular orbitals in the surface-bound state were found to directly correlate with cyclic voltammetry data in aqueous solution.

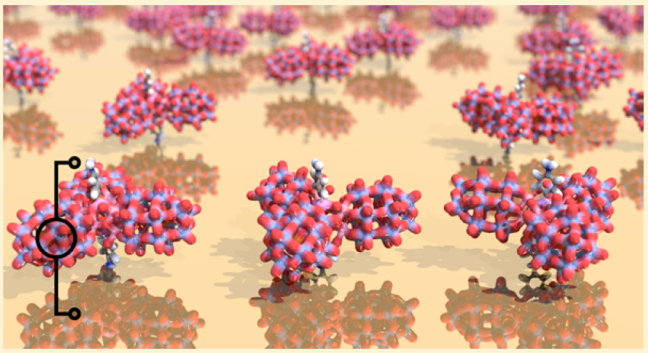

INTRODUCTION

Highly energy-efficient molecular spintronics is emerging as a rapidly growing field due to the prospects of the combined exploitation of molecular charge and spin states.[1] Polyoxometalates (POMs) as discrete nanoscale metal-oxo clusters able to incorporate magnetic centers in their structures offer a number of advantages for creating molecular spintronic devices, such as thermal and redox stability coupled with large structural diversity and tunability of the magnetic properties.[2] One of the key challenges to fabricate molecular devices is control over molecular anchoring on the surfaces of metallic electrodes in terms of spatial molecular orientation as well as the degree of electronic interactions between the metallic surface states and the molecular orbitals.[3] As such, understanding the electronic consequences caused by the interactions of magnetically functionalized POMs with metal substrates is essential to their eventual use in molecular spintronics. We here elaborate a POM-based model system that allows us to assess and compare the molecular frontier orbitals that are accessible in molecular charge transport measurements for a surface-adsorbed POM via independent methods, namely, transient voltage spectroscopy and cyclic voltammetry.

A possible step toward this goal relies on the prefunctionalization of a magnetic molecule with "glue groups" (e.g., −SH, $-N_2^+$, $-NH_2$, etc.) that covalently bind, or chemisorb, to a specific surface. In recent years it was demonstrated that such groups can be introduced into POM species by attachment of various organic ligands, e.g., alkoxides, siloxanes, and organo-(bis)phosphonates and -arsonates,[4−6] although examples of functionalized magnetic POMs are still scarce,[5] despite the prospect that POM functionalization with glue groups has already enabled well-ordered patterning of various surfaces.[6]

Here we explore a novel surface anchoring mode (organo-amino group–Au surface) in an approach to render magnetically functionalized POMs accessible to charge transport experiments in distinct environments, in solution as well as in surface-adsorbed monolayers. For the design of our target

Received: July 6, 2017
Published: September 13, 2017

DOI: 10.1021/jacs.7b07034
J. Am. Chem. Soc. 2017, 139, 14501−14510

molecules we exploited the fact that organoarsonates on one hand can provide a robust tetrahedral arsonate site that often can be readily integrated as a part of a magnetic core of transition metal ions, e.g., to replace phosphate groups possessing a terminal oxygen (see ref 7 for some examples of POMs containing such HPO_4^{-} groups). On the other hand, starting with phenylarsonate, as an easily accessible model ligand, one can further introduce various functional substituents to the phenyl ring (e.g., $-NH_2$ groups in *meta*- or *para*-positions).

Until now no magnetic organoarsonate−polyoxotungstate derivatives have been reported, although several magnetic bisphosphonates-containing POMs are known,[5] e.g., $[\{(B\text{-}\alpha\text{-}PW_9O_{34})Co_3(OH)(H_2O)_2(Ale)_2\}_2Co]^{14-}$ (H_5Ale = $(^{+}H_3N\text{-}(CH_2)_3)(OH)C(PO_3H_2)_2$), which was shown to exhibit single-molecule magnet features and is composed of two $\{B\text{-}\alpha\text{-}PW_9O_{34}Co_3\}$ subunits connected via an additional Co^{II} center as well as two alendronate ligands.[5a]

Our efforts resulted in isolation of two novel species with general formula $[Co^{II}_9(H_2O)_6(OH)_3(p\text{-}RC_6H_4AsO_3)_2(\alpha\text{-}P_2W_{15}O_{56})_3]^{25-}$, where R is either H (**1**) or NH_2 (**2**), which were crystallized as hydrated sodium salts $Na_{25}[Co_9(H_2O)_6(OH)_3(p\text{-}RC_6H_4AsO_3)_2(\alpha\text{-}P_2W_{15}O_{56})_3]\cdot 86H_2O$ (**Na-1** and **Na-2**, respectively) and characterized in the solid state and aqueous solutions. We also carried out surface deposition studies on bare gold surfaces for the amino-terminated polyanion **2**, which are of particular interest, as to date the amine-containing molecule self-assembled monolayers (SAMs) on Au were less studied in comparison with thiol-containing SAMs.[8]

RESULTS AND DISCUSSION

Synthesis. The polyanions were prepared by reacting $CoCl_2$, phenylarsonic (for **1**) or *p*-arsanilic (for **2**) acid, and the trilacunary Wells−Dawson-type polyoxotungstate (POT) salt $Na_{12}[\alpha\text{-}P_2W_{15}O_{56}]\cdot 24H_2O$[9] in 0.66 M CH_3COOH/CH_3COONa buffer solution (pH 5.2) at 60 °C for 4 days. Plate-like brown crystals of $Na_{16-x}H_x[(H_2O)_2Co_4(\alpha\text{-}P_2W_{15}O_{56})_2]\cdot nH_2O$ (**Na-3**), based on the well-known sandwich-type polyanion $[(H_2O)_2Co_4(\alpha\text{-}P_2W_{15}O_{56})_2]^{16-}$ (**3**),[10] form as the first product during evaporation of the reaction solution and should be repeatedly removed by filtration. Further evaporation of the obtained filtrate within several days leads to pink needle-like (or elongated plate-like) crystals of **Na-1** or **Na-2**. The crystalline materials of **Na-1** and **Na-2** should be collected within 1 to 2 days after formation to prevent their contamination with **Na-3** side-product. The use of any larger amounts of Co^{II} ions (than specified in the synthetic procedures) during the synthesis of **Na-1** or **Na-2** leads to the presence of Co^{II} as countercations and thus should be prevented. The influence of other synthetic reaction parameters on the formation of **1** and **2** is discussed after the structural description.

Crystal Structures. Single-crystal X-ray structural analysis of **Na-1** and **Na-2** revealed that polyanions **1** and **2** display a similar molecular structure based on a $\{Co^{II}_9(H_2O)_6(OH)_3(p\text{-}RC_6H_4AsO_3)_2\}$ core (Co_9L_2, where L = $C_6H_5AsO_3^{2-}$ for **1** and $p\text{-}H_2NC_6H_4AsO_3^{2-}$ for **2**, Figure 1c), stabilized by three $[\alpha\text{-}P_2W_{15}O_{56}]^{12-}$ POT moieties (Figure 1a,b).

Alternatively, the core structure of **1** and **2** can be viewed as a C_{3h}-symmetric trimer of $\{Co_3(H_2O)_2P_2W_{15}O_{56}\}$ units (that can be considered as trisubstituted $\{M_{18}P_2O_{56}\}$ Wells−Dawson-type phosphotungstates) linked together by three OH groups and two phenylarsonate or *p*-arsanilate ligands. **1** and **2** represent equilateral triangular structures with side lengths of ca. 2.2 nm and a thickness (maximum extension of the organoarsonates groups) of ca. 1.7 nm. Each Co^{II} ion in the $\{Co_3(H_2O)_2P_2W_{15}O_{56}\}$ building block resides in an octahedral coordination environment and coordinates to one μ_4-O (3Co, P) of the inner phosphate group (Co−O: 2.166(14)−2.268(13) Å for **1**, 2.156(14)−2.239(14) Å for **2**) and two μ_2-O (Co, W) atoms (Co−O: 2.014(14)−2.109(12) Å for **1**, 2.014(14)−2.100(14) Å for **2**) of a $\{P_2W_{15}\}$ subunit. One of the three Co^{II} ions additionally coordinates two μ_3-O, linking it with two other Co^{II} centers and the As^{V} center of the phenylarsonate or *p*-arsanilate ligand (Co−O: 2.038(13)−2.119(13) Å for **1**, 2.048(14)−2.093(14) Å for **2**) as well as a μ_3-OH group that connects it to two Co^{II} ions of the neighboring $\{Co_3(H_2O)_2P_2W_{15}O_{56}\}$ unit (Co−O: 2.041(13)−2.146(13) Å for **1**, 2.048(14)−2.093(14) Å for **2**).

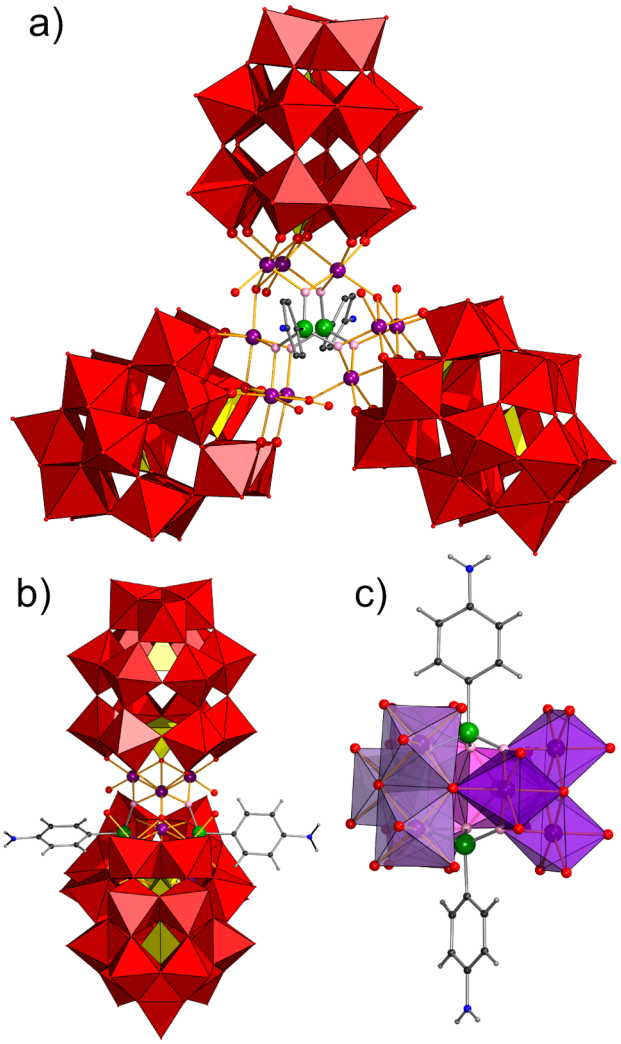

Figure 1. Structure of polyanion **2** in front (a; H atoms omitted for clarity) and side (b) views. (c) Structure of the $\{Co_9(p\text{-}ars)_2\}$ core, with CoO_6 coordination spheres shown as transparent purple octahedra. Color code: WO_6, red octahedra; PO_4, yellow tetrahedra; As, green; Co, purple; C, black; N, blue; H, gray; O, red spheres; O sites belonging to O_3As groups are shown in pink; bonds in the phenylarsonate or *p*-arsanilate groups are in gray; Co−O bonds in orange.

DOI: 10.1021/jacs.7b07034
J. Am. Chem. Soc. 2017, 139, 14501−14510

The other two Co^{II} ions bind to a terminal aqua ligand (Co–O: 2.111(15)–2.135(14) Å for **1**, 2.087(16)–2.157(15) Å for **2**), one above-mentioned μ_3-oxygen of the phenylarsonate/*p*-arsanilate and a μ_3-OH group linking them to each other and to a Co^{II} of the third $\{Co_3(H_2O)_2P_2W_{15}O_{56}\}$ moiety (Figure 1a). The protonation sites (bridging OH and terminal H_2O ligands) are confirmed by bond valence sum calculations (Tables S1, S2). The P–O and W–O bonds in **1** and **2** are typical for POTs. As–O bonds amount to 1.659(12) to 1.685(12) Å for **1** and 1.680(13) to 1.704(15) Å for **2**, while As–C bonds are 1.89(2)–1.918(13) Å (**1**) and 1.93(2) Å (**2**). The two phenylarsonate/*p*-arsanilate ligands in **1**/**2** are located on the opposite sides of the $\{Co_9(H_2O)_6(OH)_3(\alpha\text{-}P_2W_{15}O_{56})_3\}$ assembly, with their (*p*-amino)phenyl groups oriented along the C_3 axis of the inorganic core structure (Figure 1b,c). These organic groups also eliminate all symmetry elements of polyanions **1** and **2**; the dihedral angle between the two phenyl rings is 81.8(7)° in **1** and 39.4(7)° in **2**. Overall, the structure of the $\{Co_9(H_2O)_6(OH)_3L_2(\alpha\text{-}P_2W_{15}O_{56})_3\}$ assemblies in **1** and **2** is reminiscent of $[Co_9(H_2O)_6(OH)_3(HPO_4)_2(\alpha\text{-}P_2W_{15}O_{56})_3]^{25-}$ (**4**) reported several years ago by the Cronin group,[7e] where two hydrogen phosphate groups are present instead of phenylarsonate or *p*-arsanilate. The central $\{Co_9(H_2O)_6(OH)_3(HPO_4)_2\}$ core is also present in $[Co_9(H_2O)_6(OH)_3(HPO_4)_2(PW_9O_{34})_3]^{16-}$ polyanions,[7a–c] which were shown to catalyze heterogeneous water oxidation[11a–c] while stabilized by Keggin-type $\{PW_9O_{34}\}$-type POTs, along with several other Co(II)-based POTs.[11d–h]

We note that already back in 1984 Weakley predicted the possibility to replace terminal oxygen in each of the two external phosphate groups by alkyl or aryl groups for POM functionalization.[7a] Our findings support a general strategy that uses organoarsonate ligands for functionalization of magnetic polyanions incorporating tetrahedral phosphate or arsenate groups with terminal oxo/hydroxo groups. We also explored similar reactions with organophosphonates (e.g., phenylphosphonate); this however only resulted in the formation of the hydrated sodium salts of the known phosphate-based POMs **4**, $Na_xH_{25-x}[Co_9(H_2O)_6(OH)_3(HPO_4)_2(\alpha\text{-}P_2W_{15}O_{56})_3]\cdot nH_2O$ (**Na-4**).[12] Formation of **Na-4** was also observed by reacting $CoCl_2$, phenylarsonate (or *p*-arsanilate), and $\{P_2W_{15}\}$ in 1 M LiCl at higher pH values (8–10) or in a $Na_2CO_3/NaHCO_3$ buffer solution (pH 9.4). We hypothesize that the high pH of the reaction medium leads to partial $\{P_2W_{15}\}$ decomposition and the release of free phosphate required for formation of **4**. Also addition of dimethylammonium chloride (DMACl) or CsCl to our reaction mixtures for preparation of **1** and **2** results in crystallization of polyanions **4** rather than DMA or Cs salts of the desired products. Thus, pH and counterion size play a crucial role in the isolation of **1** and **2** over nonfunctionalized **4**.

As expected, IR spectra of **Na-1** and **Na-2** (Figure S1) are similar and exhibit a set of three peaks characteristic for P–O vibrations at 1084, 1042, and 1011 cm^{-1} for **Na-1** and 1086, 1042, and 1009 cm^{-1} for **Na-2**, comparable to the peaks in the IR spectrum of $Na_{12}[\alpha\text{-}P_2W_{15}O_{56}]\cdot 24H_2O$ at 1130, 1086, and 1009 cm^{-1}. The disappearance of the band at 1130 cm^{-1} and appearance of the band at 1042 cm^{-1} are in agreement with coordination of the O atom of the PO_4 group at the lacunary site of the $\{P_2W_{15}\}$ ligand by three Co^{II} ions in **1** and **2**. The bands at 933 (**Na-1**) and 932 cm^{-1} (**Na-2**) correspond to W=O vibrations. Peaks at 880, 806, 731, 598, 525, and 459 cm^{-1} (**Na-1**) and 881, 806, 725, 600, 521, and 457 cm^{-1} (**Na-2**) are associated with W–O–W, W–O–Co, and W–O–P bond vibrations. The remarkable shift of these bands compared to W–O–W bands in noncoordinated $\{P_2W_{15}\}$ (see Figure S1) is consistent with the coordination of Co^{II} to $\{P_2W_{15}\}$ in **Na-1** and **Na-2**. The characteristic As–O bands (800–815 cm^{-1})[13] overlap with W–O–W/Co/P modes (strong band at 806 cm^{-1}). Overlap also affects As–C, C–C, and C–H vibrations of the organic moieties in **Na-1** and **Na-2** in the POT region. However, C–C and C–H vibrations result in weak bands between 1600 and 1100 cm^{-1} (Figure S1). Characteristic of **Na-2** is the sharp C–N band at 1352 cm^{-1}.

We have additionally performed ATR FT-IR measurements on a saturated solution of **Na-2** in H_2O in comparison to the solid **Na-2** sample. The good match of the spectra (Figure S3) suggests solution stability of polyanions **2** in aqueous medium, at least within the duration of the measurement.

Thermogravimetrical Analysis. The thermal stability of **Na-1** and **Na-2** was investigated in the range of 25–900 °C under a N_2 atmosphere. The TGA curves of both compounds are similar (Figures S4, S5) and exhibit a major mass loss in several consecutive nonresolved steps up to 300 °C due to the release of 86 lattice water molecules per formula unit (10.6% observed vs 10.8% calcd for **Na-1**, 10.3% obsd vs 10.8% calcd for **Na-2**). Several additional steps in the 300–690 °C range are attributed to the loss of six coordinated water molecules and three hydroxo ligands, combined with decomposition and removal of phenyl (**Na-1**) or *p*-aminophenyl (**Na-2**) groups of the $p\text{-}RC_6H_4AsO_3^{2-}$ ligands as well as with O_2 release due to reduction of As^V ions (2.5% obsd vs 1.7% calcd for **Na-1** and 2.6% obsd vs 1.8% calcd for **Na-2**). Additional decrease in mass between 700 and 800 °C may stem from loss of volatile arsenic oxide (e.g., as incomplete release of 0.5 As_4O_6 per formula unit: 0.8% expt vs 1.4% calcd (**Na-1**) and 0.6% obsd vs 1.4% calcd (**Na-2**)). The total mass loss at 900 °C is 14.0% for **Na-1** and 13.8% for **Na-2**.

Magnetochemical Analysis. The magnetic data of **Na-1** and **Na-2** are shown as $\chi_m T$ vs T and M_m vs B curves in Figure 2 (molar magnetic susceptibility χ_m, molar magnetization M_m, temperature T, and magnetic field B). At 290 K, the $\chi_m T$ value of **Na-1** is 25.98 cm^3 K mol^{-1} at 0.1 T, i.e., in the range of 20.81–30.43 cm^3 K mol^{-1} expected for nine noninteracting, octahedrally coordinated high-spin Co^{II} centers.[14] Upon lowering T, $\chi_m T$ decreases, initially slowly ($T \geq 180$ K) and subsequently rapidly, down to 3.37 cm^3 K mol^{-1} at 2.0 K. At

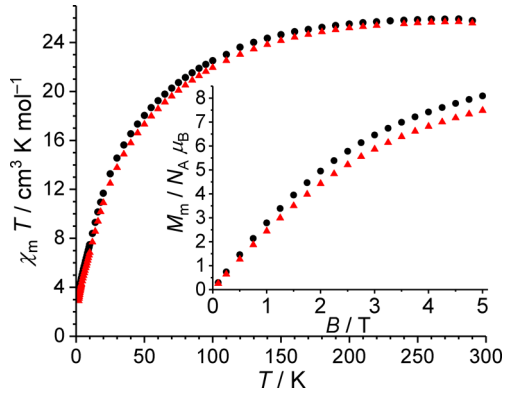

Figure 2. Temperature dependence of $\chi_m T$ at 0.1 T of **Na-1** (black circles) and **Na-2** (red triangles). Insets: Molar magnetization M_m vs applied field B at 2.0 K.

DOI: 10.1021/jacs.7b07034
J. Am. Chem. Soc. 2017, 139, 14501–14510

this temperature, the molar magnetization M_m is almost linear with the applied field up to ca. 2 T. For higher fields, the magnetization subsequently increases with continuously decreasing slope, yielding 8.1 N_A μ_B at 5.0 T, well below the expected saturation value of 30.0−36.3 N_A μ_B for nine noninteracting Co^{II} centers. Both curves thus reveal predominant antiferromagnetic exchange interactions between the nine Co^{II} centers in **1**. While the rapid decrease of $\chi_m T$ upon cooling below ∼100 K, is, for the most part, due to these exchange interactions, the $\chi_m T$ vs T curve is also effected by the ligand field of each single Co^{II} center causing a similar contribution that distinctly deviates from the spin-only behavior in the range 2.0−180 K. This is due to the thermal depopulation of the energy states originating from the $^4T_{1g}$ ground multiplet of the ^4F ground term that is further split by spin−orbit coupling contributions, in particular due to mixing with the states originating from the excited $^4T_{1g}(^4P)$ multiplet.[15]

The magnetic data of **Na-2** and **of Na-1** match almost perfectly. Taking into account the structure of both compounds, the slight differences of the characteristic values (**Na-2**: at 0.1 T, $\chi_m T$ = 25.75 cm^3 K mol^{-1} at 290 K and 2.91 cm^3 K mol^{-1} at 2.0 K; M_m = 7.6 N_A μ_B at 5.0 T and 2.0 K) are potentially due to the slightly different exchange coupling mediated by the organoarsonate ligands, but the differences might also be caused by minor paramagnetic impurities. Nevertheless, the conclusions drawn from the magnetochemical analysis of **Na-1** are the same for **Na-2**.

A quick comparison of the magnetic data of **Na-1** and **Na-2** to **Na-4**[7e] reveals extensive resemblance. The shapes of the $\chi_m T$ *vs* T and M_m vs B curves are very similar, while their magnitudes are different. This may be caused by the different ligands (organoarsonate (**Na-1**, **Na-2**) vs phosphate groups (**Na-4**)). The magnitude of deviation (about 25%) is, however, surprisingly large, which rather points to an uncertainty in the molar mass (as scaling factor), i.e., a different amount of a diamagnetic component such as crystal water within the measured sample. The samples used for magnetic measurements thus were subsequently characterized by TGA; however, the results are the same as presented above. In addition, compounds **Na-1**, **Na-2**, and **Na-4** do not show out-of-phase ac susceptibility signals down to 1.8 K and up to 1000 Hz.

UV−Vis Spectroscopy. Aqueous solutions of **Na-1** and **Na-2** (Figures S6, S8) show similar absorption spectra that exhibit a strong maximum at around 200 nm (215 nm for **Na-1** and 195 nm for **Na-2**) followed by an absorption maximum at around 260 nm (which is well-resolved for **Na-1** and is overlapped with the first absorption peak for **Na-2**) in the UV light area and a less intense absorption maximum at 532 nm in the visible light area. The spectrum remains unchanged for at least 18 h, confirming the short-term stability of polyanions in aqueous solutions (Figure S9), in line with the conclusions obtained from the Diamond ATR-FTIR measurements.

Electrochemical Studies. We have recorded cyclic voltammograms for 0.7 mM **Na-1**, **Na-2**, **Na-3**, and **Na-4** solutions in 0.5 M CH_3COONa buffer (pH 4.8). The electrochemical behavior of the three Co_9-based POMs (**1**, **2** and **4**) is very similar. The cyclic voltammograms for these species exhibit four redox couples attributed to reduction and reoxidation of the W^{VI} centers of the POT ligands between −0.50 and −1.05 V vs Ag/AgCl (Figures 3, S10, Table 1). At potentials below −1.05 V a reduction of solvent occurs, coupled with formation of a film on the glassy carbon electrode. In comparison to the electrochemical activity of the sandwich-type

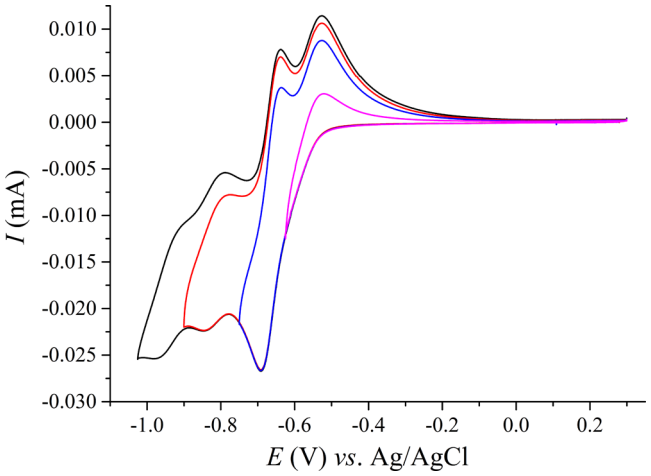

Figure 3. Room-temperature cyclic voltammograms of a 0.7 mM solution of **Na-1** in 0.5 M CH_3COONa buffer (pH 4.8) with different negative potential limits (−0.625, −0.75, −0.95, and −1.025 V) at a scan rate of 20 mV/s.

polyanions **3** in the same medium, exhibiting three well-defined redox waves before hydrogen evolution (Table 1, Figure S11), reduction of W^{VI} centers in the Co_9-based species takes place at more negative potentials showing higher redox stability of the latter. The peak currents for the redox processes in **1**−**4** are proportional to the square root of the scanning rate, which is characteristic for diffusion-controlled electrode reactions. At higher pH (6.4) all redox waves are shifted toward more negative potentials (Figure S12), indicating that the reduction of tungsten(VI) ions is coupled with proton transfer, as it is common for POTs.[16] Correspondingly, only three redox waves are accessible for **2** in the pH 6.4 medium before hydrogen evolution. No reversible redox waves associated with Co^{II} oxidation in the $\{Co_9L_2\}$ core could be observed in the positive potential range at both pH 4.8 and 6.4.

The CV curves of **1**, **2**, and **4** remain unchanged for several hours; however after 1 day an additional shoulder centered at around −0.50 V appears, while there are also other slight changes in relative intensities and shape of the other redox waves. The shoulder at −0.50 V looks very similar to the first redox wave observed for **3** in the same medium (Figure S13). These changes are accompanied by a color change of the POM solutions from pink to light-brown. These observations imply partial decomposition of the $\{Co_9L_2(P_2W_{15})_3\}$ POMs in 0.5 M sodium acetate buffer (pH 4.8) followed by formation of the $\{Co_xNa_{4-x}(P_2W_{15})_2\}$ species; this is also in agreement with the presence of **Na-3** as a common side-product during the synthesis of **Na-1** and **Na-2**.

Formation and Characterization of Self-Assembled Monolayer. We investigated the electron transport properties of a molecular device based on the amine-terminated polyanions **2**. For this purpose, we prepared SAMs of **2** on flat bare template-stripped gold surface (Au^{TS})[17] and characterized it using ellipsometry, FT-IRRAS, X-ray photoemission spectroscopy (XPS), cyclic voltammetry (CV), and conducting tip atomic force microscopy (C-AFM) measurements.

It was found that the incubation of the freshly prepared gold surface in the aqueous solution of **Na-2** (10^{-3} M in DI water) during 24 h leads to the formation of a layer with a thickness between 1.4 ± 0.2 and 2.0 ± 0.2 nm (measured on two batches,

DOI: 10.1021/jacs.7b07034
J. Am. Chem. Soc. 2017, 139, 14501−14510

Table 1. Electrochemical Data for the Polyanions 1−4 in 0.5 M CH_3COONa Buffer (pH 4.8)[a]

POM	$E_{1/2}^{I}$, V	$E_{1/2}^{II}$, V	$E_{1/2}^{III}$, V	$E_{1/2}^{IV}$, V
1	−0.57 ± 0.04	−0.67 ± 0.03	−0.82 ± 0.03	−0.94 ± 0.03
2	−0.56 ± 0.07	−0.67 ± 0.04	−0.82 ± 0.03	−0.94 ± 0.03
4	−0.58 ± 0.07	−0.67 ± 0.05	−0.80 ± 0.02	−0.92 ± 0.03
3	−0.50 ± 0.08	−0.70 ± 0.06	−0.89 ± 0.06	

[a]The potentials are given vs Ag/AgCl reference electrode at a 20 mV/s scan rate.

see Experimental Part), which is consistent with the expected thickness of the polyoxoanion monolayer in the most probable orientation on the gold surface shown in Figure S14 (~1.7 nm according to the XRD data). The thickness of the obtained layer did not change after ultrasonic cleaning of the sample in water, indicating a high stability of the POM SAM.

The results of topographic AFM in contact mode (Figure S15) further suggest the homogeneity of the obtained layer. The root-mean-square (RMS) roughness of 0.31 nm (RMS roughness is defined here as the square root of the arithmetic mean of the squares of each z value measured on an AFM image) obtained by AFM is in a good agreement with a standard deviation of 0.2 nm observed by ellipsometry. This value is also well comparable with the RMS roughness of the template-stripped (TS) Au surface before grafting molecules measured at the same conditions, which is around 0.5 nm. However, we note that AFM images reveal some pinholes with a diameter of a few tens of nm and apparent depth of about 1 nm (about half the total SAM thickness, although the exact value cannot be determined due to AFM tip convolution effect).

The obtained POM-covered surface was also characterized by CV. The three-electrode cell setup was used with a POM-covered gold surface as the working electrode, Pt wire as a counter electrode, and Ag/AgCl (saturated KCl) as a reference electrode (Figure S16). The characteristic wave of the successive one-electron reduction process attributed to **2** on the gold surface (black line, Figure S16) was identified at ca. −0.38 V vs Ag/AgCl (saturated KCl), but it is not well-defined and appears irreversible. We also perform CV measurements of the **Na-2** in the same electrolyte solution we used for CV studies of the POM-containing surface for comparison (red line, Figure S16). For this measurement Pt wires acted as working and counter electrodes, whereas Ag/AgCl (saturated KCl) was used as a reference electrode.

The XPS experiments of the **Na-2** SAM on gold (Figure S17) show distinctive photoemission lines of W $4f_{7/2}$ (36.2 eV) and W $4f_{5/2}$ (38.4 eV), As 3d (42.0 and 45.5 eV), C 1s (284.8 eV), and Co 2p (~782 eV, almost invisible). The results are confirmed by XPS measurements of the **Na-2** powder sample, which also reveal photoemission peaks of the other elements of interest (Figure S18). Due to its low content and relatively low photoionization cross sections, a very weak photoemission peak of N 1s (~401 eV) is present just at the detection limit of the experiment and hints at a broadening and splitting indicative of attachment of the amino group to the Au substrate. Doublets of P 2p (~136 eV) and Co 2p (~781 eV) for the powder sample are significantly stronger comparing to the **Na-2** on Au, which is aligned with our expectations. A semiquantitative analysis of the photoemission lines belonging to Co, Na, P, W, and C was performed using the SESSA simulation package.[18] The analysis confirms the powder retains its stoichiometry. Photoelectron cross sections values were taken from ref 19, and inelastic mean free path was calculated using the TPP-2 formula.[20]

Interestingly, the Na 1s peak was not observed for a **Na-2** SAM on gold, in contrast to the XPS data for bulk material (~1073 eV for **Na-2** powder).

Additionally, a thin layer of **Na-2** immobilized on an Au surface from an aqueous solution was characterized by FT-IRRAS (Figure S19). The measurement reveals several characteristic peaks that further support uniform **Na-2** immobilization on the Au surface. Thus, the bands at 821 cm^{-1} as well as at 919 cm^{-1} are most likely vibrations of W−O−W, Co−O−W, and P−O−W bonds, while that at 1108 cm^{-1} corresponds to vibrations of the P−O bonds. They are slightly shifted as compared to the peaks detected by FT-IR measurements in transmission of **Na-2** powder (806, 881 cm^{-1}; and 1086 cm^{-1}, respectively). This shift is expected due to the different sample forms and measurement methods that lead to variant vibration frequencies.[21] The numerous rotational−vibrational transitions observed between 2000 and 1200 cm^{-1} should be owing to the hydrophilic nature of **Na-2**, the high amount of crystal water present in this compound, and the preparation of the sample from ultrapure water.

Current−voltage (I−V) curves were measured by electrically contacting the SAM by C-AFM. Figure 4a shows the 2D

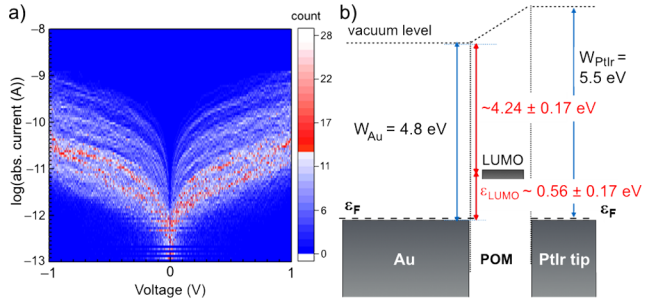

Figure 4. (a) 2D current histogram of 325 I−V curves measured by C-AFM (at a loading force of 30 nN) on the SAM of **2** chemically grafted on an ultraflat template stripped gold electrode (Au^{TS}). Voltages applied on the Au^{TS} electrode (C-AFM grounded). (b) Schematic energy diagram of the Au^{TS}/POM/PtIr C-AFM tip as deduced from both the I−V and CV measurements.

histograms of around 300 I−V curves (see Experimental Part). The I−V curves are dispersed over about three decades, as shown by current histograms at a given bias (e.g., +0.9 and −0.9 V, Figure S20). This dispersion is large when compared to similar C-AFM measurements of alkylthiol SAMs on Au (here about 3 decades vs about 1[22]) or π-conjugated molecules.[23] The I−V curves are symmetric with respect to the voltage polarity. The current histograms are fitted by two Gaussian peaks (Figure S20), and the mean values of the current histograms (Figure S20) are ca. 1.82×10^{-11} A/1.6×10^{-10} A (two peaks) at 0.9 V and ca. 1.9×10^{-11} A/2.1×10^{-10} A at −0.9 V. The results have been reproduced in a second batch of SAMs (see Figures S22−S24).

DOI: 10.1021/jacs.7b07034
J. Am. Chem. Soc. 2017, 139, 14501−14510

Table 2. Crystal Data and Structure Refinement for Na-1 and Na-2

	Na-1	Na-2
empirical formula	$C_{12}H_{197}As_2Co_9Na_{25}O_{269}P_6W_{45}$	$C_{12}H_{199}As_2Co_9N_2Na_{25}O_{269}P_6W_{45}$
fw, g mol^{-1}	14 360.73	14 390.76
cryst syst	triclinic	triclinic
space group	$P\bar{1}$	$P\bar{1}$
a, Å	25.8088(3)	14.2262(2)
b, Å	25.8336(3)	24.8597(4)
c, Å	27.1598(3)	37.9388(4)
α, deg	78.1282(11)	81.9672(10)
β, deg	61.7276(14)	87.8161(10)
γ, deg	60.6220(14)	76.5409(12)
volume, Å^3	13888.9(3)	12920.6(3)
Z	2	2
D_{calc}, g/cm^3	3.434	3.699
absorp coeff, mm^{-1}	19.496	20.958
$F(000)$	12 850	12 882
cryst size, mm^3	0.08 × 0.23 × 0.81	0.11 × 0.16 × 0.51
theta range for data collection	4.08−25.35°	4.08−25.68°
completeness to θ_{max}	99.5%	99.5%
index ranges	$-31 \le h \le 30$, $-31 \le k \le 31$, $-32 \le l \le 32$	$-17 \le h \le 17$, $-30 \le k \le 30$, $-45 \le l \le 46$
reflns collected	259 838	248 406
indep reflns	50 595	48 866
R_{int}	0.0981	0.0799
obsd ($I > 2\sigma(I)$)	36 674	41 474
absorption corr	analytical using a multifaceted crystal model	
T_{min}/T_{max}	0.0201/0.3081	0.0159/0.2120
data/restraints/params	50 595/60/1941	48 866/54/2189
goodness-of-fit on F^2	1.057	1.142
R_1, wR_2 ($I > 2\sigma(I)$)	R_1 = 0.0614, wR_2 = 0.1450	R_1 = 0.0643, wR_2 = 0.1374
R_1, wR_2 (all data)	R_1 = 0.0923, wR_2 = 0.1698	R_1 = 0.0771, wR_2 = 0.1443
largest diff peak and hole, e Å^{-3}	5.061 and −4.591	4.614 and −4.239

We can infer several possible origins for this large dispersion:

(1) Disorder in the SAMs. For example, in some cases multipeaks and consequently a larger dispersion can be observed for disordered SAMs over two decades of current.[24] This large dispersion can also be due to the presence of "defects" (such as pinholes; see above and Figure S15) with reduced thickness and thus larger current through the SAMs. Thus, the two peaks in the current histograms can be ascribed to zones of different molecular organizations in the SAMs.

(2) Intermolecular interaction ($\pi-\pi$ interactions) between neighboring molecules, which can broaden the conductance histograms.[25]

We also analyze the $I-V$ curves with the TVS (transient voltage spectroscopy) method[26] to estimate the energy position (with respect to the Fermi energy of the electrodes) of the molecular orbital (HOMO or LUMO) involved in the charge transport process (Figure 4b). From the minima of the TVS plots (Figure S21), we deduced (see Experimental Part) a LUMO at ca. (0.56 ± 0.17) eV above the electrode Fermi energy (energy diagram Figure 4b) or at (4.24 ± 0.17) eV below the vacuum level (considering a work function of Au^{TS} at 4.8 eV). This later value is consistent with the LUMO position determined from CV on the SAM, the reduction peak at −0.38 V giving a LUMO at −4.2 eV below the vacuum level (see equation in the Experimental Part). This consistency between $I-V$ and CV measurements indicates a weak or moderate electronic coupling between the molecules and the Au surface (through the phenyl amine groups) on one side and through the C-AFM tip mechanical contact on the other side.

EXPERIMENTAL PART

General Methods and Materials. Reagents were used as purchased without further purification. $Na_{12}[\alpha\text{-}P_2W_{15}O_{56}]\cdot 24H_2O$ was obtained according to the reported procedure[9] starting from $K_6[\alpha\text{-}P_2W_{18}O_{62}]\cdot 14H_2O$.[27] Elemental analysis results (ICP-OES and C, H, N) were obtained from Central Institute for Engineering, Electronics and Analytics (ZEA-3), Forschungszentrum Jülich GmbH (D-52425 Jülich, Germany). TGA/DTA measurements were carried out with a Mettler Toledo TGA/SDTA 851 in dry N_2 (60 mL min^{-1}) at a heating rate of 5 K min^{-1}. Vibrational spectra were recorded on a Bruker VERTEX 70 FT-IR spectrometer coupled with a RAM II FT-Raman module (1064 nm Nd:YAG laser) on KBr disks for the FT-IR and the solid material for the Diamond ATR-FTIR and Raman measurements. Liquid-phase ATR-FTIR spectra were obtained on a saturated **Na-2** solution in H_2O. UV−vis spectra were measured using 10 mm quartz cuvettes on an Analytik Jena Specord S600 spectrophotometer.

Synthesis of $Na_{25}[Co_9(OH)_3(H_2O)_6(C_6H_5AsO_3)_2(P_2W_{15}O_{56})_3]\cdot 86H_2O$ (Na-1). $Na_{12}[\alpha\text{-}P_2W_{15}O_{56}]\cdot 24H_2O$ (0.221 g, 0.05 mmol), $CoCl_2$ (0.023 g, 0.175 mmol), and $C_6H_5AsO_3H_2$ (0.010 g, 0.05 mmol) were dissolved in 6 mL of 0.66 M CH_3COONa buffer (pH 5.2)[28]

DOI: 10.1021/jacs.7b07034
J. Am. Chem. Soc. 2017, 139, 14501−14510

under vigorous stirring in an oil bath at 60 °C for 4 days. The reaction mixture was then filtered, divided into several vials, and left for evaporation at room temperature. Brown plate-like crystals of the side-product $Na_{16-x}H_x[(H_2O)_2Co_4(P_2W_{15}O_{56})_2]\cdot nH_2O$ (**Na-3**) start to appear immediately after cooling the reaction mixture to room temperature. They have to be removed by filtration, and filtration of **Na-3** has to be repeated in the next few days. Pure dark-pink crystals of **Na-1** form after 2 weeks. The crystals were collected by filtration, washed with 0.66 M CH_3COONa buffer, and dried in air. Yield: 0.016 mg (6.6% based on $\{P_2W_{15}\}$). Anal. Calcd for $C_{12}H_{197}Co_9Na_{25}O_{269}P_6As_2W_{45}$ (found): C, 1.00 (1.04); H, 1.38 (1.38); Co, 3.69 (3.70); Na, 4.00 (4.00); P, 1.29 (1.29); As, 1.04 (1.03); W, 57.61 (55.7) %. IR (KBr pellet), cm^{-1}: 3454 (s, br); 1632 (s); 1439 (w); 1418 (w); 1385 (w); 1352 (w); 1084 (s); 1042 (m); 1011 (m); 933 (s); 912 (s); 880 (s); 806 (s); 731 (s); 598 (m); 561 (m); 525 (m); 492 (m); 459 (m). Raman (in solid), cm^{-1}: 977 (s); 956 (s); 880 (m); 816 (m); 523 (w); 370 (m); 121 (m). UV−vis (H_2O): λ = 215 nm, $\varepsilon = 2.45 \times 10^7$ M^{-1} cm^{-1}; λ = 265 nm, $\varepsilon = 1.06 \times 10^7$ M^{-1} cm^{-1}; λ = 532 nm, $\varepsilon = 3.67 \times 10^5$ M^{-1} cm^{-1}. UV−vis (0.5 M CH_3COONa solution, pH 5.1): λ = 235 nm, $\varepsilon = 3.21 \times 10^9$ M^{-1} cm^{-1}; λ = 531 nm, $\varepsilon = 3.88 \times 10^5$ M^{-1} cm^{-1}.

Synthesis of $Na_{25}[Co_9(OH)_3(H_2O)_6(H_2NC_6H_4AsO_3)_2(P_2W_{15}O_{56})_3]\cdot 86H_2O$ (Na-2). $Na_{12}[\alpha\text{-}P_2W_{15}O_{56}]\cdot 24H_2O$ (0.221 g, 0.05 mmol), $CoCl_2$ (0.023 g, 0.175 mmol), and $H_2NC_6H_4AsO_3H_2$ (0.011 g, 0.05 mmol) were dissolved in 6 mL of 0.66 M CH_3COONa buffer (pH 5.2)[28] under vigorous stirring in an oil bath at 60 °C for 4 days. Then the resulting reaction mixture was filtered, divided into several vials, and left for evaporation at room temperature. Brown plate-like crystals of the side product $Na_{16-x}H_x[(H_2O)_2Co_4(P_2W_{15}O_{56})_2]\cdot nH_2O$ (**Na-3**) start to form immediately after cooling the reaction mixture and have to be removed by filtration after the reaction and on the next day. Pink needle-like crystals of **Na-2** form after 2 days. They were collected by filtration, washed with 0.66 M CH_3COONa buffer, and dried in air. Yield: 0.0075 mg (3.1% based on $\{P_2W_{15}\}$). Anal. Cald for $C_{12}H_{199}N_2Co_9Na_{25}O_{269}P_6As_2W_{45}$ (found): C, 1.00 (1.09); H, 1.39 (1.37); N, 0.19 (0.19); Co, 3.69 (3.73); Na, 3.99 (3.93); P, 1.29 (1.33); As, 1.04 (1.09); W, 57.49 (57.67)%. IR (KBr pellet), cm^{-1}: 3449 (s, br); 1626 (s); 1504 (w); 1470 (w); 1383 (w); 1354 (w); 1321 (w); 1292 (w); 1264 (w), 1194 (w); 1142 (m); 1086 (s); 1042 (m); 1009 (m); 932 (s); 910 (s), 881 (s); 806 (s); 725 (s); 600 (m); 561 (m); 521 (s); 457 (m). Raman (in solid), cm^{-1}: 978 (s); 957 (s); 916 (m), 905 (m), 893 (m), 883 (m); 839 (m); 523 (w). UV−vis (H_2O): λ = 195 nm, $\varepsilon = 1.23 \times 10^8$ M^{-1} cm^{-1}; λ = 255 nm, $\varepsilon = 3.01 \times 10^7$ M^{-1} cm^{-1}; λ = 532 nm, $\varepsilon = 6.60 \times 10^4$ M^{-1} cm^{-1}.

X-ray Crystallography. Single-crystal diffraction data for **Na-1** and **Na-2** were collected on a SuperNova (Agilent Technologies) diffractometer with Mo Kα radiation (λ = 0.710 73 Å) at 120 K. Crystals were mounted in a Hampton cryoloop with Paratone-N oil to prevent water loss. Absorption corrections were applied numerically based on a multifaceted crystal model using CrysAlis software.[29] The SHELXTL software package[30] was used to solve and refine the structure. The structures were solved by direct methods and refined by full-matrix least-squares method against $|F|^2$ with anisotropic thermal parameters for all heavy atoms (W, P, Co, Na).

The hydrogen atoms of the phenyl rings in **Na-1** and **Na-2** and the amino groups in **Na-2** were placed in geometrically calculated positions. The hydrogens of the water molecules and OH groups were not located. The relative site occupancy factors for the disordered positions of Na^+ countercations and oxygen atoms of cocrystallized solvent water molecules were first refined in an isotropic approximation with U_{iso} = 0.05 and then fixed at the obtained values and refined without the thermal parameter restrictions.

One of the P_2W_{15} ligands in the **Na-2** structure was disordered with a 95:5% ratio between the two components. The disorder was modeled using a combination of PART and EADP instructions. The rather high value still remaining for the second weighting term (650 for **Na-1** and 1420 for **Na-2**) most likely reflects the large volume occupied by highly disordered solvate and is consistent with large solvent-accessible volume remaining in the structures. Severe disorder did not allow localizing the positions for all the Na cations and O atoms of crystal waters in **Na-1**. Thus, only 16.5 Na^+ ions and 60 cocrystallized H_2O molecules have been found from the X-ray data for this compound, while 25 Na^+ and 86 crystal waters are present as based on elemental and thermogravimetrical analyses (TGA). For the overall consistency, the final formula in the CIF file of **Na-1** corresponds to the composition of the bulk material determined by elemental analysis and TGA, as all further studies were performed on the isolated well-dried bulk materials of **Na-1**. The number of counterions and cocrystallized solvent molecules found in the crystal structure for **Na-2** was consistent with those determined by other analytical techniques.

Additional crystallographic data are summarized in Table 2. Further details on the crystal structure investigation can be obtained, free of charge, on application to CCDC, 12 Union Road, Cambridge CB2 1EZ, UK: http://www.ccdc.cam.ac.uk/, e-mail: data_request@ccdc.cam.ac.uk, or fax: + 441223 336033 upon quoting 1552113 (**Na-1**) and 1552114 (**Na-2**) numbers.

Magnetic Measurements. These were performed using a Quantum Design MPMS-5XL SQUID magnetometer. The polycrystalline samples were compacted and immobilized into cylindrical PTFE capsules. In static magnetic field, data were acquired as a function of the magnetic field (0.1−5.0 T at 2.0 K) and temperature (2.0−290 K at 0.1 T). Dynamical field (ac) data were collected in the absence of a static bias field in the frequency range 1−1500 Hz (T = 2.0−50 K, B_{ac} = 3 G); however, no out-of-phase signals were detected. Data were corrected for the diamagnetic contributions of sample holder and compound (**Na-1**: $\chi_{dia} = -7.18 \times 10^{-3}$ cm^3 mol^{-1}, **Na-2**: $\chi_{dia} = -7.20 \times 10^{-3}$ cm^3 mol^{-1}).

Cyclic Voltammograms of 1−4. These were recorded in aqueous media using a Bio Logic SP-150 potentiostat controlled via EC-Lab software. The conventional three-electrode electrochemical cell included a glassy carbon working electrode with a diameter of 3 mm, a platinum wire counter electrode, and an aqueous Ag/AgCl (3 M NaCl) reference electrode (0.196 V vs SHE determined by measuring $[Fe(CN)_6]^{3-/4-}$ as an internal standard). The solutions were thoroughly deaerated with pure argon and kept under a positive Ar pressure during the experiments. Alumina powder was used for the cleaning of the working electrode, which was then thoroughly rinsed with deionized water. Redox potentials were determined from the average values of the anodic and cathodic peak potentials and reported vs Ag/AgCl (3 M NaCl) reference electrode.

Template-Stripped Au Substrates. Very flat Au^{TS} surfaces were prepared according to the method reported by the Whiteside's group.[17] In brief, a 300−500 nm thick Au film is evaporated on a very flat silicon wafer covered by its native SiO_2 (RMS roughness of 0.4 nm), which was previously carefully cleaned by piranha solution (30 min in 2:1 H_2SO_4/H_2O_2 (v/v); ***Caution**: Piranha solution is exothermic and strongly reacts with organics*), rinsed with deionized (DI) water, and dried under a stream of nitrogen. A clean glass piece (ultrasonicated in acetone for 5 min, ultrasonicated in 2-propanol for 5 min, and UV-irradiated in ozone for 10 min) is glued (UV polymerizable glue) on the evaporated Au film and mechanically stripped with the Au film attached on the glass piece (Au film is cut with a razor blade around the glass piece). This very flat (RMS roughness of 0.4 nm, the same as the SiO_2 surface used as template) and clean template-stripped Au^{TS} surface is immediately used for the formation of the molecule self-assembled monolayer.

Spectroscopic Ellipsometry. We recorded spectroscopic ellipsometry data in the visible range using a UVISEL (Jobin Yvon Horiba) spectroscopic ellipsometer equipped with DeltaPsi 2 data analysis software. The system acquired a spectrum ranging from 2 to 4.5 eV (corresponding to 300 to 750 nm) with intervals of 0.1 eV (or 15 nm). Data were taken at an angle of incidence of 70°, and the compensator was set at 45.0°. Data were fitted by a regression analysis to a film-on-substrate model as described by their thickness and their complex refractive indexes. First, a background before monolayer deposition for the gold-coated substrate was recorded. Second, after the monolayer deposition, we used a two-layer model (substrate/SAM) to fit the measured data and to determine the SAM thickness. We employed the previously measured optical properties of the gold-coated substrate

DOI: 10.1021/jacs.7b07034
J. Am. Chem. Soc. 2017, 139, 14501−14510

(background), and we fixed the refractive index of the organic monolayer at 1.50. The usual values in the literature for the refractive index of organic monolayers are in the range 1.45−1.50.[31] We can notice that a change from 1.50 to 1.55 would result in less than 1 Å error for a thickness less than 30 Å. We estimated the accuracy of the SAM thickness measurements at ±2 Å.

IRRAS Measurements. These were performed on a Bruker Vertex 70 FT-IR spectrometer equipped with a high-sensitivity Hg−Cd−Te (MCT) detector and an A513/Q variable-angle reflection accessory including an automatic rotational holder for the MIR polarizer. The IR beam was polarized with a KRS-5 polarizer with 99% degree of polarization. Double-sided interferograms were collected with a sample frequency of 20 kHz, an aperture of 1.5 mm, and a nominal spectral resolution of 4 cm^{-1}. The interferograms were apodized by a Blackmann−Harris three-term apodization and zero-filled with a zero-filling factor of 2. The angle of incidence was set to 80°, and p-polarized IR radiation was used to record the spectra. For the background measurements, the sample chamber was purged with argon for 5 min; then 1024 scans were collected while continuing to purge. For the sample measurements, argon purging was started at the moment the first scan was recorded. The scans were averaged until the peaks arising from the water vapor in the sample chamber were compensated, for which typically 800−1500 scans were necessary. Where necessary, scattering correction was applied to the spectra.

General Procedure for the Preparation of Au Substrates for IRRAS. Au substrates were fabricated by sputtering a 10 nm adhesive film of Ti and a 100 nm thick layer of Au on ⟨100⟩-oriented silicon wafers with a native SiO_2 layer. The freshly prepared Au substrates were cleaned in oxygen plasma [$p(O_2)$ = 0.4 mbar, f = 40 kHz, and P = 75 W] for 4 min immediately prior to the **Na-2** deposition. For the deposition, a low concentrated solution (∼0.4 mmol) of the **Na-2** sample was prepared using ultrapure water with a conductivity of <55 nS cm^{-1}. The Au substrate was stored for 24 h in this solution, then washed with a small amount of ultrapure water and dried for 24 h in a desiccator.

Cyclic Voltammograms of 2 on Gold. CV experiments were performed with a Modulab potentiostat from Solartron Analytical and a classical three-electrode electrochemical cell. The SAM-covered Au^{TS} electrode was used as the working electrode. The counter electrode was a platinum wire (0.5 mm), and Ag/AgCl (saturated KCl) was used as a reference electrode (REF). The CV curve was recorded at a scan rate of 100 mV/s. The energy position (with respect to vacuum) of the LUMO of the SAM was estimated from the first reduction peak E_{red} by $E_{LUMO} = -(E_{red} + E_{REF/SHE}) - 4.24$[32] in eV with $E_{REF/SHE}$ = 0.196 V for the Ag/AgCl reference electrode.

XPS Experiments of 2 on Gold. These were performed to analyze the chemical composition of the obtained layer on gold and to detect any unremoved contaminant. We used a Physical Electronics 5600 spectrometer fitted in a UHV chamber with a residual pressure of 2 × 10^{-10} Torr. High-resolution spectra were recorded with a monochromatic Al Kα X-ray source ($h\nu$ = 1486.6 eV), a detection angle of 45° as referenced to the sample surface, an analyzer entrance slit width of 400 μm, and an analyzer pass energy of 12 eV. In these conditions, the overall resolution as measured from the full-width at half-maximum of the Ag $3d_{5/2}$ line is 0.55 eV. The spectra were recalibrated with respect to the C 1s peak at 284.8 eV. Semi-quantitative analyses were completed after standard background subtraction according to Shirley's method.[33] Peaks were decomposed by using Voigt functions and a least-squares minimization procedure and by keeping constant the Gaussian and Lorentzian broadenings for each component of a given peak.

XPS Experiments of the Reference Powder Sample of Na-2. These were carried out using the Specs Phoibos-150 energy analyzer and a non-monochromatized Al Kα X-ray source, with an overall energy resolution of 0.9 eV. The energy calibration of XPS measurements was done by aligning of the C 1s core level peak to 284.8 eV. The spectra were analyzed after Shirley background subtraction, with exceptions of Co 2p, N 1s, and As 3p + P 2p regions, where the linear background was used instead. Spectra were decomposed using Voigt-function shapes, and fitting employed the KolXPD analysis package. Small charging effects were observed; the C 1s core-level exhibits an asymmetry, and it was decomposed into two symmetrical Voigt components (287.1 and 288.5 eV). The energy axis of measurements was left unmodified.

C-AFM Measurements and TVS Analysis. We performed current−voltage measurements by C-AFM in ambient air (ICON, Bruker), using a PtIr-coated tip (tip radius of curvature less than 25 nm, force constant in the range 0.17−0.2 N/m). Placing the conducting tips at a stationary point contact formed nanojunctions. A square grid of 10 × 10 is defined with a lateral step of 2 nm. At each point, 10 $I-V$ curves are acquired (back and forth), leading to the measurements of 1000 $I-V$ traces. Out of these 1000 $I-V$ traces, some were removed (main causes: no current−bad tip contact, noise larger than average current−tip contact fluctuations, too high current, e.g., short-circuit or pinhole in the SAM, inducing saturation of the current preamplifier), leading to about 300 useful $I-V$ traces (exact number indicated in the related figures). The load force was adjusted in the range 20−30 nN and measured by force−distance curves with the controlling software of the ICON. The bias was applied on the Au^{TS} substrate, and the tip was grounded through the input of the current amplifier. The voltage sweeps (back and forth) were applied from 0 to 1 V and then from 0 to −1 V.

The $I-V$ curves are analyzed by the TVS method.[26] In brief, the $I-V$ data are plotted as $\ln(I/V^2)$ vs $1/V$. A minimum in this curve corresponds to a transition from a direct tunneling electron transport through the molecules and a resonant tunneling via a frontier molecular orbital (LUMO or HOMO). The energy position ε_0 of the orbital involved in the transport mechanism with respect to the Fermi energy of the metal electrode is given by

$$|\varepsilon_0| = 2\frac{e|V_{T+}V_{T-}|}{\sqrt{{V_{T+}}^2 + 10|V_{T+}V_{T-}|/3 + {V_{T-}}^2}}$$

where e is the electron charge and V_{T+} and V_{T-} are the voltage of the minima of the TVS plot at positive and negative voltages, respectively.[34]

CONCLUSIONS

In summary, we suggest a general strategy for functionalization of polyoxometalates by integration of organoarsonates as prosthetic coligands to polyoxotungstate units, which can also stabilize polynuclear magnetic cores. Depending on the terminal organoarsonate residue, this can enable their attachment to metallic electrode surfaces, which we intend to explore in the context of molecular electronics and spintronics. Two corresponding polyanions with external phenyl and *para*-aminophenyl groups have been prepared and characterized in the solid state and in solution. The derivative comprising terminal amino groups was anchored to a Au surface, and the thus-obtained SAM was extensively characterized via ellipsometry, FT-IRRAS, XPS, cyclic voltammetry, and C-AFM measurements. This study thereby proves the recently suggested suitability of the $-NH_2$ functional group for direct binding of molecules to noble metal surfaces (e.g., Au^0) without a mercaptocarboxylate link commonly used for this purpose. Electron transport measurements by C-AFM show a relatively large dispersion of the current through the molecular junctions, corresponding to the polyoxotungstate-centered LUMO orbitals located between ca. 0.4 and 0.7 eV above the Fermi energy of the Au electrode. The presence of the second amino group not bound to the metal substrate in principle can also be used for postfunctionalization of the formed SAM that we plan to explore in follow-up work.

DOI: 10.1021/jacs.7b07034
J. Am. Chem. Soc. 2017, 139, 14501−14510

■ ASSOCIATED CONTENT

Supporting Information

The Supporting Information is available free of charge on the ACS Publications website at DOI: 10.1021/jacs.7b07034.

Bond valence sum values; (ATR)-IR, Raman, UV−vis, XPS and IRRAS spectra; TGA curves, further CV details, AFM image, current histograms and TVS plots for SAM of **2** on Au surface, and packing diagrams for **Na-1** and **Na-2** (PDF)

Crystallographic data for **Na-1** (CIF)

Crystallographic data for **Na-2** (CIF)

■ AUTHOR INFORMATION

Corresponding Authors

*dominique.vuillaume@iemn.fr

*paul.koegerler@ac.rwth-aachen.de

ORCID

Stéphane Lenfant: 0000-0002-6857-8752

Slavomír Nemšák: 0000-0002-6103-2925

Paul Kögerler: 0000-0001-7831-3953

Notes

The authors declare no competing financial interest.

■ ACKNOWLEDGMENTS

We gratefully acknowledge financial support by Forschungszentrum Jülich, EU ERC Starting Grant 308051−MOLSPINTRON (P.K.) and COST Action CM 1203 (M.S.). We thank Brigitte Jansen for TGA measurements and Dr. Volkmar Heß for fruitful discussions.

■ REFERENCES

(1) See for example: (a) Sanvito, S.; Rocha, A. R. *J. Comput. Theor. Nanosci.* **2006**, *3*, 624−642. (b) Bogani, L.; Wernsdorfer, W. *Nat. Mater.* **2008**, *7*, 179−188. (c) Osorio, E. A.; Bjørnholm, T.; Lehn, J.-M.; Ruben, M.; van der Zant, H. S. J. *J. Phys.: Condens. Matter* **2008**, *20*, 374121−14. (d) Sanvito, S. *Chem. Soc. Rev.* **2011**, *40*, 3336−3355. (e) Fahrendorf, S.; Atodiresei, N.; Besson, C.; Caciuc, V.; Matthes, F.; Blügel, S.; Kögerler, P.; Bürgler, D. E.; Schneider, C. M. *Nat. Commun.* **2013**, *4*, 2425−6. (f) Perrin, M. L.; Burzurí, E.; van der Zant, H. S. J. *Chem. Soc. Rev.* **2015**, *44*, 902−919 and references therein.

(2) See for example: (a) Lehmann, J.; Gaita-Ariño, A.; Coronado, E.; Loss, D. *Nat. Nanotechnol.* **2007**, *2*, 312−317. (b) Fang, X.; Kögerler, P. *Chem. Commun.* **2008**, 3396−3398. (c) Kortz, U.; Müller, A.; van Slageren, J.; Schnack, J.; Dalal, N. S.; Dressel, M. *Coord. Chem. Rev.* **2009**, *253*, 2315−2327. (d) Kögerler, P.; Tsukerblat, B.; Müller, A. *Dalton Trans.* **2010**, *39*, 21−36. (e) Clemente-Juan, J. M.; Coronado, E.; Gaita-Ariño, A. *Chem. Soc. Rev.* **2012**, *41*, 7464−7478. (f) Song, Y. F.; Tsunashima, R. *Chem. Soc. Rev.* **2012**, *41*, 7384−7402. (g) Izarova, N. V.; Kögerler, P. In *Trends in Polyoxometalates Research*; Ruhlmann, L., Schaming, D., Eds.; Nova Science Publishers: Hauppauge, 2015; pp 121−149. (h) Ji, Y. C.; Huang, L. J.; Hu, J.; Streb, C.; Song, Y. F. *Energy Environ. Sci.* **2015**, *8*, 776−789. (i) Busche, C.; Vilà-Nadal, L.; Yan, J.; Miras, H. N.; Long, D.-L.; Georgiev, V. P.; Asenov, A.; Pedersen, R. H.; Gadegaard, N.; Mirza, M. M.; Paul, D. J.; Poblet, J. M.; Cronin, L. *Nature* **2014**, *515*, 545−549. (j) Palii, A.; Tsukerblat, B.; Clemente-Juan, J. M.; Coronado, E. *J. Phys. Chem. C* **2016**, *120*, 16994−17005. (k) Shiddiq, M.; Komijani, D.; Duan, Y.; Gaita-Ariño, A.; Coronado, E.; Hill, S. *Nature* **2016**, *531*, 348−351. (l) Linnenberg, O.; Moors, M.; Solé-Daura, A.; López, X.; Bäumer, C.; Kentzinger, E.; Pyckhout-Hintzen, W.; Monakhov, K. Yu. *J. Phys. Chem. C* **2017**, *121*, 10419−10429.

(3) (a) Lissel, F.; Schwarz, F.; Blacque, O.; Riel, H.; Lörtscher, E.; Venkatesan, K.; Berke, H. *J. Am. Chem. Soc.* **2014**, *136*, 14560−14569. (b) Monakhov, K. Yu.; Moors, M.; Kögerler, P. *Adv. Inorg. Chem.* **2017**, *69*, 251−286 and references therein.

(4) See for example: (a) Dolbecq, A.; Dumas, E.; Mayer, C. R.; Mialane, P. *Chem. Rev.* **2010**, *110*, 6009−6048. (b) Proust, A.; Matt, B.; Villanneau, R.; Guillemot, G.; Gouzerh, P.; Izzet, G. *Chem. Soc. Rev.* **2012**, *41*, 7605−7622. (c) Santonia, M.-P.; Hanana, G. S.; Hasenknopf, B. *Coord. Chem. Rev.* **2014**, *281*, 64−85 and references therein.

(5) See for example: (a) El Moll, H.; Dolbecq, A.; Marrot, J.; Rousseau, G.; Haouas, M.; Taulelle, F.; Rogez, G.; Wernsdorfer, W.; Keita, B.; Mialane, P. *Chem. - Eur. J.* **2012**, *18*, 3845−3849. (b) El Moll, H.; Zhu, W.; Oldfield, E.; Rodriguez-Albelo, M.; Mialane, P.; Marrot, J.; Vila, N.; Mbomekallé, I. M.; Rivière, E.; Duboc, C.; Dolbecq, A. *Inorg. Chem.* **2012**, *51*, 7921−7931. (c) Rousseau, G.; Rivière, E.; Dolbecq, A.; Marrot, J.; Oms, O.; Mialane, P. *Eur. J. Inorg. Chem.* **2013**, *2013*, 1793−1798. (d) Saad, A.; Zhu, W.; Rousseau, G.; Mialane, P.; Marrot, J.; Haouas, M.; Taulelle, F.; Dessapt, R.; Serier-Brault, H.; Rivière, E.; Kubo, T.; Oldfield, E.; Dolbecq, A. *Chem. - Eur. J.* **2015**, *21*, 1−12. (e) Saad, A.; Anwar, N.; Rousseau, G.; Mialane, P.; Marrot, J.; Haouas, M.; Taulelle, F.; Mc Cormac, T.; Dolbecq, A. *Eur. J. Inorg. Chem.* **2015**, *2015*, 4775−4782. (f) Xue, H.; Zhao, J.-W.; Pan, R.; Yang, B.-F.; Yang, G.-Y.; Liu, H.-S. *Chem. - Eur. J.* **2016**, *22*, 12322−12331. (g) Ban, R.; Sun, X.; Wang, J.; Ma, P.; Zhang, C.; Niu, J.; Wang, J. *Dalton Trans.* **2017**, *46*, 5856−5863.

(6) See for example: (a) Joo, N.; Renaudineau, S.; Delapierre, G.; Bidan, G.; Chamoreau, L. M.; Thouvenot, R.; Gouzerh, P.; Proust, A. *Chem. - Eur. J.* **2010**, *16*, 5043−5051. (b) Musumeci, C.; Luzio, A.; Pradeep, C. P.; Miras, H. N.; Rosnes, M. H.; Song, Y.-F.; Long, D.-L.; Cronin, L.; Pignataro, B. *J. Phys. Chem. C* **2011**, *115*, 4446−4455. (c) Mercier, D.; Boujday, S.; Annabi, C.; Villanneau, R.; Pradier, C.-M.; Proust, A. *J. Phys. Chem. C* **2012**, *116*, 13217−13224. (d) Rinfray, C.; Izzet, G.; Pinson, J.; Gam Derouich, S.; Combellas, C.; Kanoufi, F.; Proust, A. *Chem. - Eur. J.* **2013**, *19*, 13838−13846. (e) Derouich, S. G.; Rinfray, C.; Izzet, G.; Pinson, J.; Gallet, J.-J.; Kanoufi, F.; Proust, A.; Combellas, C. *Langmuir* **2014**, *30*, 2287−2296. (f) Yvon, C.; Surman, A. J.; Hutin, M.; Alex, J.; Smith, B. O.; Long, D.-L.; Cronin, L. *Angew. Chem.* **2014**, *126*, 3404−3409. (g) Volatron, F.; Noël, J.-M.; Rinfray, C.; Decorse, P.; Combellas, C.; Kanoufi, F.; Proust, A. *J. Mater. Chem. C* **2015**, *3*, 6266−6275. (h) Lombana, A.; Rinfray, C.; Volatron, F.; Izzet, G.; Battaglini, N.; Alves, S.; Decorse, P.; Lang, P.; Proust, A. *J. Phys. Chem. C* **2016**, *120*, 2837−2845.

(7) See for example: (a) Weakley, T. J. R. *J. Chem. Soc., Chem. Commun.* **1984**, 1406−1407. (b) Galán-Mascarós, J. R.; Gómez-García, C. J.; Borrás-Almenar, J. J.; Coronado, E. *Adv. Mater.* **1994**, *6*, 221−223. (c) Clemente-Juan, J. M.; Coronado, E.; Galán-Mascarós, J. R.; Gómez-García, C. J. *Inorg. Chem.* **1999**, *38*, 55−63. (d) Ritchie, C.; Boyd, T.; Long, D.-L.; Ditzel, E.; Cronin, L. *Dalton Trans.* **2009**, 1587−1592. (e) Lydon, C.; Sabi, M. M.; Symes, M. D.; Long, D.-L.; Murrie, M.; Yoshii, S.; Nojirib, H.; Cronin, L. *Chem. Commun.* **2012**, *48*, 9819−9821.

(8) (a) Quek, S. Y.; Venkataraman, L.; Choi, H. J.; Louie, S. G.; Hybertsen, M. S.; Neaton, J. B. *Nano Lett.* **2007**, *7*, 3477−3482. (b) de la Llave, E.; Clarenc, R.; Schiffrin, D. J.; Williams, F. J. *J. Phys. Chem. C* **2014**, *118*, 468−475. (c) Koo, K. M.; Sina, A. A. I.; Carrascosa, L. G.; Shiddiky, M. J. A.; Trau, M. *Anal. Methods* **2015**, *7*, 7042−7054.

(9) Contant, R. *Inorg. Synth.* **1990**, *27*, 106−111.

(10) Finke, R. G.; Droege, M. W. *Inorg. Chem.* **1983**, *22*, 1006−1008.

(11) (a) Goberna-Ferrón, S.; Vigara, L.; Soriano-López, J.; Galán-Mascarós, J. R. *Inorg. Chem.* **2012**, *51*, 11707−11715. (b) Soriano-López, J.; Goberna-Ferrón, S.; Vigara, L.; Carbó, J. J.; Poblet, J. M.; Galán-Mascarós, J. R. *Inorg. Chem.* **2013**, *52*, 4753−4755. (c) Goberna-Ferrón, S.; Soriano-López, J.; Galán-Mascarós, J. R.; Nyman, M. *Eur. J. Inorg. Chem.* **2015**, *2015*, 2833−2840. (d) Yin, Q.; Tan, J. M.; Besson, C.; Geletii, Y. V.; Musaev, D. G.; Kuznetsov, A. E.; Luo, Z.; Hardcastle, K. I.; Hill, C. L. *Science* **2010**, *328*, 342−345. (e) Zhu, G.; Geletii, Y. V.; Kögerler, P.; Schilder, H.; Song, J.; Lense, S.; Zhao, C.; Hardcastle, K. I.; Musaev, D. G.; Hill, C. L. *Dalton Trans.* **2012**, *41*, 2084−2090. (f) Lv, H.; Song, J.; Geletii, Y. V.; Vickers, J. W.; Sumliner, J. M.; Musaev, D. G.; Kögerler, P.; Zhuk, P.; Bacsa, J.; Zhu,

G.; Hill, C. L. *J. Am. Chem. Soc.* **2014**, *136*, 9268−9271. (g) Soriano-López, J.; Musaev, D. G.; Hill, C. L.; Galán-Mascarós, J. R.; Carbó, J. J.; Poblet, J. M. *J. Catal.* **2017**, *350*, 56−63. (h) Song, F.; Ding, Y.; Ma, B.; Wang, C.; Wang, Q.; Du, X.; Fua, S.; Song, J. *Energy Environ. Sci.* **2013**, *6*, 1170−1184.

(12) Unit cell for $Na_xH_{25-x}[Co_9(H_2O)_6(OH)_3(HPO_4)_2(\alpha\text{-}P_2W_{15}O_{56})_3]\cdot nH_2O$ (**Na-4**): triclinic, $P\bar{1}$, a = 13.9486(4) Å, b = 29.2148(7) Å, c = 31.7155(8) Å, α = 74.603(2)°, β = 81.760(2)°, γ = 89.949(2)°, V = 12320.2(5) Å^3, Z = 2.

(13) Barsukova, M.; Izarova, N. V.; Ngo Biboum, R.; Keita, B.; Nadjo, L.; Ramachandran, V.; Dalal, N. S.; Antonova, N. S.; Carbó, J. J.; Poblet, J. M.; Kortz, U. *Chem. - Eur. J.* **2010**, *16*, 9076−9085.

(14) Lueken, H. *Magnetochemie*; Teubner: Stuttgart, 1999.

(15) (a) Ballhausen, C. *Introduction to Ligand-Field Theory*; McGraw-Hill: New York, 1962. (b) Figgs, N. B.; Hitchman, M. A. *Ligand-Field Theory and its Applications*; Wiley-VCH: New York, 2000.

(16) See for example: (a) Ruhlmann, L.; Nadjo, L.; Canny, J.; Contant, R.; Thouvenot, R. *Eur. J. Inorg. Chem.* **2002**, *2002*, 975−986. (b) Lisnard, L.; Mialane, P.; Dolbecq, A.; Marrot, J.; Clemente-Juan, J. M.; Coronado, E.; Keita, B.; de Oliveira, P.; Nadjo, L.; Sécheresse, F. *Chem. - Eur. J.* **2007**, *13*, 3525−3536. (c) Ruhlmann, L.; Schaming, D.; Ahmed, I.; Courville, A.; Canny, J.; Thouvenot, R. *Inorg. Chem.* **2012**, *51*, 8202−8211. (d) Duan, Y.; Clemente-Juan, J. M.; Giménez-Saiz, C.; Coronado, E. *Inorg. Chem.* **2016**, *55*, 925−938.

(17) Weiss, E.; Chiechi, R.; Kaufman, G.; Kriebel, J.; Li, Z.; Duati, M.; Rampi, M.; Whitesides, G. *J. Am. Chem. Soc.* **2007**, *129*, 4336−4349.

(18) Smekal, W.; Werner, W. S. M.; Powell, C. J. *Surf. Interface Anal.* **2005**, *37*, 1059.

(19) Yeh, J. J.; Lindau, I. *At. Data Nucl. Data Tables* **1985**, *32*, 1−155.

(20) Tanuma, S.; Powell, C. J.; Penn, D. R. *Surf. Interface Anal.* **1994**, *21*, 165.

(21) Allara, D. L.; Baca, A.; Pryde, C. A. *Macromolecules* **1978**, *11*, 1215−1220.

(22) (a) Engelkes, V. B.; Beebe, J. M.; Frisbie, C. D. *J. Phys. Chem. B* **2005**, *109*, 16801−16810. (b) Kim, T.-W.; Wang, G.; Lee, H.; Lee, T. *Nanotechnology* **2007**, *18*, 315204.

(23) Smaali, K.; Lenfant, S.; Karpe, S.; Oçafrain, M.; Blanchard, P.; Deresmes, D.; Godey, S.; Rochefort, A.; Roncali, J.; Vuillaume, D. *ACS Nano* **2010**, *4*, 2411−2421.

(24) Smaali, K.; Clément, N.; Patriarche, G.; Vuillaume, D. *ACS Nano* **2012**, *6*, 4639−4647.

(25) (a) Reuter, M. G.; Hersam, M. C.; Seideman, T.; Ratner, M. A. *Nano Lett.* **2012**, *12*, 2243−2248. (b) Trasobares, J.; Rech, J.; Jonckheere, T.; Martin, T.; Aleveque, O.; Levillain, E.; Diez-Cabanes, V.; Olivier, Y.; Cornil, J.; Nys, J. P.; Sivakumarasamy, R.; Smaali, K.; Leclere, P.; Fujiwara, A.; Théron, D.; Vuillaume, D.; Clément, N. *Nano Lett.* **2017**, *17*, 3215−3224.

(26) (a) Beebe, J. M.; Kim, B.; Gadzuk, J. W.; Frisbie, C. D.; Kushmerick, J. G. *Phys. Rev. Lett.* **2006**, *97*, 026801. (b) Ricœur, G.; Lenfant, S.; Guérin, D.; Vuillaume, D. *J. Phys. Chem. C* **2012**, *116*, 20722−20730.

(27) Contant, R. *Inorg. Synth.* **1990**, *27*, 105−106.

(28) The 0.66 M CH_3COONa buffer (pH 5.2) was prepared by dissolving 41 g of CH_3COONa and 9.14 mL of glacial CH_3COOH in 1000 mL of H_2O.

(29) *CrysAlisPro*; Agilent Technologies, 1.171.36.28 (release 01-02-2013 CrysAlis171.NET).

(30) Sheldrick, G. M. *Acta Crystallogr., Sect. A: Found. Crystallogr.* **2008**, *A64*, 112−122.

(31) (a) Ulman, A. *An Introduction to Ultrathin Organic Films: From Langmuir-Blodgett to Self-assembly*; Academic Press: Boston, 1991. (b) Parikh, A. N.; Allara, D. L.; Ben Azouz, I.; Rondelez, F. *J. Phys. Chem.* **1994**, *98*, 7577−7590.

(32) Cardona, C. M.; Li, W.; Kaifer, A. E.; Stockdale, D.; Bazan, G. C. *Adv. Mater.* **2011**, *23*, 2367−2371.

(33) Shirley, D. A. *Phys. Rev. B* **1972**, *5*, 4709−4714.

(34) Bâldea, I. *Phys. Rev. B: Condens. Matter Mater. Phys.* **2012**, *85*, 035442.

DOI: 10.1021/jacs.7b07034
J. Am. Chem. Soc. 2017, 139, 14501−14510